Enhancing Aerospace Fault Diagnosis With Conditioned Multiscale Generative Adversarial Networks

Lihao Ye, Ke Zhang, *Senior Member, IEEE*, Bin Jiang, *Fellow, IEEE*, and Silvio Simani, *Senior Member, IEEE*

***Abstract*—In the aerospace field, equipment failures can lead to substantial economic losses and pose significant safety risks, making effective fault diagnosis crucial. Traditional fault diagnosis methods typically require large, precisely labeled datasets, which are challenging to obtain in aerospace applications due to the rarity and unpredictability of faults. To overcome these limitations, this article proposes a novel conditioned multiscale generative adversarial networks (GANs) approach designed to enhance fault diagnosis performance under small-sample conditions. Initially, raw vibration signals undergo preprocessing using the short-time Fourier transform, which expands frequency-domain features while preserving essential time-frequency characteristics. Subsequently, conditioned multiscale GANs are trained on these limited datasets, employing multiscale convolutional kernels to extract and fuse rich features, thus generating high-quality synthetic samples. Finally, these synthetic samples are combined with the original dataset to train a convolutional neural network offline, which can subsequently perform real-time online fault diagnosis. Extensive validation on two aerospace-related datasets demonstrates that the proposed method significantly enhances fault diagnosis accuracy and efficiency, even when the available training data is severely limited.**

***Index Terms*—Deep learning, fault diagnosis, generative adversarial networks (GANs), small samples.**

I. Introduction

TIMELY and accurate fault diagnosis is critical in contemporary industrial systems to ensure operational reliability and efficiency, particularly in the aerospace sector where equipment failures can result in substantial economic losses and significant safety hazards [1], [2], [3], [4]. Consequently, the demand for advanced fault diagnosis techniques has become increasingly urgent.

Fault diagnosis approaches generally fall into two categories: 1) model-driven and 2) data-driven methods [5]. Model-driven methods rely on physical models of systems to predict and diagnose faults, typically requiring accurate system modeling and numerous parameters [6], [7], [8]. However, due to the inherent complexity and uncertainty of real-world systems, traditional model-driven techniques often encounter significant challenges related to inaccurate or incomplete system models. Conversely, data-driven methods utilize operational data to diagnose faults, extracting underlying patterns from the data without necessitating precise physical models [9], [10], [11], [12]. Data-driven approaches can swiftly and effectively predict and diagnose faults, making them particularly suitable for complex systems. Driven by rapid advancements in big data analytics and artificial intelligence, data-driven fault diagnosis methods have increasingly gained widespread acceptance, progressively replacing traditional model-driven methodologies.

Despite substantial progress in data-driven fault diagnosis, these techniques typically require large datasets for effective training. However, in the aerospace industry, fault data are frequently scarce due to the rarity and unpredictability of faults, presenting considerable obstacles to developing accurate diagnostic models. Moreover, even when fault data become available, the associated high costs and the required specialist knowledge for accurate labeling further complicate this process [13]. These dual challenges—data scarcity and labeling costs—highlight the critical need for more efficient and adaptable diagnostic techniques. Therefore, identifying underlying features in limited datasets to develop rapid and accurate diagnostic models represents a significant research direction.

To tackle these challenges, various machine learning and deep learning methods, such as transfer learning (TL) and generative adversarial networks (GANs), have been increasingly adopted. These methods have demonstrated

Received 5 May 2025; revised 25 August 2025; accepted 30 September 2025. This work was supported by the National Natural Science Foundation of China under Grant 62020106003 and Grant 62173180; in part by the Natural Science Foundation of Jiangsu Province of China under Grant BZ2024037; in part by the Aeronautical Science Foundation of China under Grant 20220057052001; and in part by the Postgraduate Research and Practice Innovation Program of Jiangsu Province under Grant KYCX25_0582. This article was recommended by Associate Editor J. Shan. *(Corresponding author: Bin Jiang.)*

Lihao Ye is with the College of Automation Engineering, Nanjing University of Aeronautics and Astronautics, Nanjing 211106, China (e-mail: lihaoye@nuaa.edu.cn).

Ke Zhang and Bin Jiang are with the College of Automation Engineering, Nanjing University of Aeronautics and Astronautics, Nanjing 211106, China, and also with the National Key Laboratory of Helicopter Aeromechanics, Nanjing 210016, China (e-mail: kezhang@nuaa.edu.cn; binjiang@nuaa.edu.cn).

Silvio Simani is with the Department of Engineering, University of Ferrara, 44122 Ferrara, Italy (e-mail: silvio.simani@unife.it).

Color versions of one or more figures in this article are available at https://doi.org/10.1109/TCYB.2025.3617108.

Digital Object Identifier 10.1109/TCYB.2025.3617108

considerable potential across different fault diagnosis scenarios [14], [15], [16]. For instance, TL has been widely adopted to enhance model generalizability across domains, while GANs have been employed to create synthetic fault samples, alleviating issues related to data scarcity. In prior research, we employed TL to realize cross-domain feature integration between source and target domains, enabling effective fault diagnosis in scenarios with class-imbalanced datasets [17]. Zhang et al. proposed a cross-domain bilateral TL (CDBTL) method under incomplete multisource domains [18]. However, TL's effectiveness is inherently constrained by the availability and quality of source domain data, as well as the degree of domain shift between source and target domains. These limitations underscore the need for complementary approaches, such as GANs, which can mitigate data scarcity by synthesizing high-quality fault samples, thereby enhancing the robustness of fault diagnosis systems. Bai et al. [19] proposed a data augmentation strategy using intertemporal return plots (IRPs), which mitigates data imbalance and enhances accuracy and convergence in fault diagnosis tasks. Yang et al. [20] applied conditional GANs (cGANs) to generate 2-D synthetic fault images, which, combined with preprocessed fault data, were subsequently used for training convolutional neural network (CNN) for online diagnosis. Although their method demonstrated efficacy, converting vibration signals into 2-D grayscale images may result in the loss of essential signal characteristics, potentially reducing diagnostic accuracy. Moreover, enhancing the resolution of generated fault images could capture more detailed features, improving model performance further.

To overcome the challenge of aerospace fault diagnosis with limited data availability, this article proposes a novel fault sample augmentation method based on time-frequency domain conditioned Multiscale GANs (c-MSGANs). The proposed method significantly expands the number of fault samples available, enabling real-time, accurate fault diagnosis even in data-scarce scenarios. The main contributions of this article are summarized as follows.

1) A novel fault sample augmentation strategy based on time-frequency domain preprocessing using short-time Fourier transform (STFT) is introduced. This approach enriches frequency-domain characteristics while retaining original time-frequency features, thereby facilitating improved feature extraction for fault diagnosis model training.
2) c-MSGANs is employed to tackle data scarcity in fault diagnosis by generating high-quality synthetic fault samples. The proposed generative approach leverages multiscale convolutional kernels to extract and fuse diverse features, significantly enhancing the dataset.
3) Synthetic fault samples generated by the proposed method are combined with original samples to train CNN. The resulting models enable rapid and highly accurate fault diagnosis in real-time.

The remainder of this article is structured as follows. Section II outlines related theories, Section III describes the proposed method, Section IV details and analyses the performance of the proposed approach through two experimental case studies, and Section V concludes the paper.

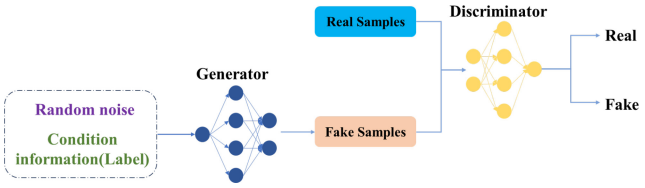

Fig. 1. Simple structure of cGANs.

II. Related Theory

A. Conditional Generative Adversarial Networks

GANs are inspired by game theory and consist of two main components: 1) the generator G and 2) the discriminator D [21]. The generator G attempts to simulate the data distribution of authentic specimens, while the discriminator D distinguishes inputs generated by G. Feedback from D to G iteratively enhances sample quality, aiming to achieve a Nash equilibrium through adversarial training [22].

The generator G aims to generate new samples by mapping random noise z through a nonlinear function. Its objective function, $\Gamma(G_{\min})$, is formulated as

$$\Gamma(G_{\min}) = \mathbb{E}_{z\sim p_z(z)}[\ln(1 - D(G(z)))] \tag{1}$$

where $p_z(z)$ denotes the distribution of the noise z, $G(z)$ represents the generated synthetic sample, and $D(G(z))$ is the discriminator's output for $G(z)$.

Equation (1) defines Γ as the objective function for G in a GANs. G seeks to minimize Γ by adjusting its parameters so that $\ln(1 - D(G(z)))$ approaches zero, thereby outsmarting D. The subscript $G_{\min}$ indicates that Γ is minimized with respect to G, reflecting the optimization process during generator training within the GANs framework.

The discriminator D, on the other hand, aims to distinguish between real and fake samples, scaling its output probability between 0 and 1. Its objective function, $\Gamma(D_{\max})$, is given by

$$\begin{aligned}\Gamma(D_{\max}) = {} & \mathbb{E}_{x\sim p_{\text{data}}(x)}[\ln D(x)] \\ & + \mathbb{E}_{z\sim p_z(z)}[\ln(1 - D(G(z)))]\end{aligned} \tag{2}$$

where $p_{\text{data}}(x)$ represents the distribution of real samples x. The objective $\Gamma(D_{\max})$ is maximized by adjusting D's parameters to maximize the sum of the expected logarithm of its output for real samples $\ln D(x)$ and the expected logarithm of $1-D(G(z))$ for samples generated by G.

For the issue of image generation, GANs present a robust solution. However, a limitation of traditional GANs is their ability to generate only random images, lacking detailed control of the results. To overcome this point, researchers have proposed cGANs. As an extension of GANs, cGANs incorporate conditional variables y into the generator and discriminator networks, thus providing control over the generation' process [23], [24]. Fig. 1 shows a basic cGANs structure.

The main concept of cGANs is the integration of a conditional information into both generator and discriminator. This arrangement allows the generation of images aligning with specific conditions, such as images of particular categories or specific styles, based on the setting of the conditional variable y. As a crucial expansion of GANs, cGANs enable conditional

control over the generation process, significantly enhancing the generative capability and applicability of the model. The objective function $V(G, D)$ is given by

$$\min_G \max_D V(\mathrm{G}, D) = \mathbb{E}_{x\sim p_{\text{data}}(x)}\left[\ln D(x|y)\right] + \mathbb{E}_{z\sim p_z(z)}\left[\ln(1 - D(G(z|y)))\right] \quad (3)$$

where y denoting the condition information, acts as a constraint within the objective function. In this context, $\mathbb{E}_{x\sim p_{\text{data}}(x)}$ represents the expectation over real data x sampled from the distribution $p_{\text{data}}(x)$, conditioned on y. Similarly, $\mathbb{E}_{z\sim p_z(z)}$ represents the expectation over noise z sampled from $p_z(z)$, with $D(x|y)$ being the discriminator's output when conditioned on y, and $D(G(z|y))$ being the discriminator's output for the generated sample $G(z|y)$.

This objective function $V(G, D)$ guides cGANs toward a min–max equilibrium. In this equilibrium, the generator G effectively learns to produce synthetic samples $G(z|y)$ that become indistinguishable from real samples conditioned on y, while simultaneously, the discriminator D refines its capability to accurately differentiate between authentic data x and generated samples $G(z|y)$.

While cGANs provide conditional control over the generation process, their performance is still constrained by the single-scale convolutional structures in both the generator and discriminator, which may limit the capacity to capture features occurring at different resolutions. To address this limitation, researchers have explored the idea of multiscale GANs, where convolutional operations at multiple receptive fields are incorporated and then fused to enhance representation learning. Building upon this idea, the multiscale GANs (MSGANs) introduces parallel convolutional branches with different kernel sizes and explicit feature fusion, enabling the generator to synthesize more diverse and realistic samples, while also stabilizing the training dynamics. In the following, we extend the cGANs framework to a c-MSGANs, which integrates conditional information into this multiscale design for improved fault-sample generation.

B. Convolutional Neural Network

CNN represent a prominent class of deep learning models specifically designed to handle data structured in grid-like arrangements [25], [26], [27]. A typical CNN architecture consists of three main types of layers: 1) convolutional layers; 2) pooling layers; and 3) fully connected layers.

The convolutional layer primarily focuses on extracting meaningful features from the input data. By applying multiple convolutional filters, distinctive patterns within the input data are captured, resulting in a set of feature maps. Mathematically, if f denotes the input image and h the convolutional kernel, the convolutional operation can be represented as

$$(f * h)(i, j) = \sum_{m=0}^{M-1}\sum_{n=0}^{N-1} f(m, n)\, h(i - m, j - n) \quad (4)$$

where (i, j) represents the spatial coordinates on the resulting feature map.

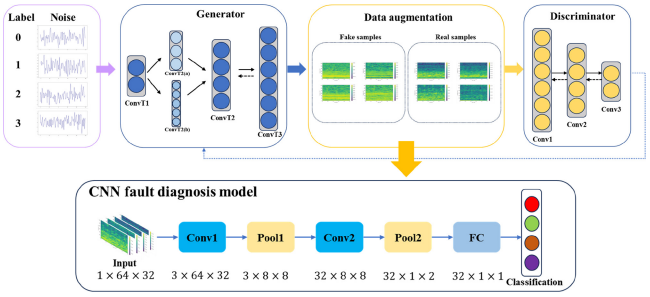

Fig. 2. Proposed c-MSGANs-CNN architecture for fault diagnosis.

Convolutional layers are usually followed by pooling layers to reduce the spatial dimensions of the feature mapping, reducing the number of parameters and computational complexity while maintaining important information. The pooling layers chosen in this article are all maximum pooling layers, and their mathematical expression is as follows:

$$\text{MaxPooling}(X) = \max(X) \quad (5)$$

where X represents the local input region from which the maximum value is selected.

The fully connected layer maps the learned "high-level" feature representations into the label space of the samples.

In this work, the Adam adaptive optimization algorithm combined with the cross-entropy loss function is employed [28]. As demonstrated by the experimental reported in [29], this specific combination facilitates effective weight updates, thereby progressively enhancing the predictive capabilities of the CNN model. Consequently, all CNN architectures presented in this article utilize this optimization approach.

Having introduced the theoretical foundations of GANs, cGANs, and CNNs, the next section describes in detail the proposed fault diagnosis method, integrating these approaches into a cohesive framework specifically designed for aerospace fault diagnosis under small-sample conditions.

III. Fault Diagnosis Method

To address the challenges of aerospace fault diagnosis under small-sample conditions, this article proposes a fault diagnosis method based on the augmentation of fault sample time-frequency images using c-MSGANs and subsequent classification through a CNN model. The overall methodology is illustrated in Fig. 2.

Specifically, Fig. 2 outlines the proposed c-MSGANs-CNN framework designed for aerospace fault diagnosis in scenarios with limited data availability. It consists of three key stages: 1) data preprocessing using STFT; 2) synthetic fault data generation with c-MSGANs; and 3) fault classification using CNN. The subsequent subsections detail each of these stages comprehensively.

A. Data Preprocessing

The STFT is a widely used technique in fault diagnosis. It is an effective tool for analyzing fault features during equipment operation [30], [31]. The STFT converts 1-D time series data

into a 2-D time-frequency matrix, making it a powerful time-frequency analysis method. The fundamental concept behind STFT involves decomposing the time-domain signal using a fixed-length window function, followed by performing a Fourier transform on each segment. This process is repeated across the time axis using a sliding window, ultimately resulting in a composite spectrum. The mathematical expression for STFT is

$$F_i(m,n)=\sum_{a=0}^{N-1} s_i(a)\cdot g^*(n-a)\cdot e^{-j\frac{2\pi}{N}\cdot ma} \tag{6}$$

where i denotes the ith sample of the channel wave signal, $g^*(\cdot)$ represents the window function, and $F_i(m,n)$ is the resulting STFT output, describing how frequency amplitude characteristics evolve over time.

While some researchers have used the approach of converting vibration signals into grayscale images for fault preprocessing, this method can lead to a loss of the original spatial significance of the data. Conversely, the STFT preserves the intrinsic characteristics of vibration signals while enhancing the frequency domain features related to faults [32], [33]. Compared to direct conversion of signals into grayscale images, STFT retains the intrinsic time-frequency distribution, which helps to capture richer fault patterns while maintaining the temporal structure of the signals.

Furthermore, the inclusion of frequency-domain information significantly enhances the interpretability of the diagnostic model, as typical mechanical faults are often associated with specific frequency bands or harmonics. This facilitates fault localization and characterization beyond mere classification accuracy, making it a valuable direction for further exploration.

Although wavelet transform (WT) is a popular method for time–frequency analysis, its performance heavily relies on the choice of wavelet basis, which introduces additional parameter tuning and potential subjectivity. In contrast, STFT is a mature and widely adopted technique in fault diagnosis, offering a fixed and interpretable time–frequency representation that integrates naturally with CNN for end-to-end learning. In our study, we adopt the STFT method for data preprocessing because it is a mainstream approach. Future work will further explore and compare various time–frequency analysis methods to enhance model generalization.

B. Data Augmentation

In this article, we proposed the c-MSGANs models trained on small sample data to augment the original dataset. The condition information used in this study corresponds to the real label information of the faults. Customized c-MSGANs structures are designed for fault information from different systems. Both the generator and discriminator networks use binary cross entropy (BCE) as their loss functions, defined mathematically as

$$\mathrm{LBCE}=-\frac{1}{N}\sum_{i=1}^{N}\left[y_i\log\left(\hat{y}_i\right)+(1-y_i)\log\left(1-\hat{y}_i\right)\right] \tag{7}$$

where N denotes the total number of samples, y_i represents the true label for the ith sample, and $\hat{y}_i$ represents the predicted probability for the ith sample.

The overall process of the proposed method is outlined in Algorithm 1. In our approach, the prefix "c" in c-MSGANs stands for "conditioned," indicating that both the generator and discriminator are provided with label information as an additional input to guide the generation process. Compared to conventional cGANs-based approaches, the c-MSGANs

Algorithm 1 c-MSGANs Algorithm

Input: Training data $\{(x_i, y_i)\}_{i=1}^{N}$, number of iterations T
Initialize: Generator parameters θ_g, Discriminator parameters θ_d
for $t = 1$ **to** T **do**
Sample mini-batch of noise samples $\{z_i\}_{i=1}^{m}$ and labels $\{y_i\}_{i=1}^{m}$
Sample mini-batch of real data $\{(x_i, y_i)\}_{i=1}^{m}$
Generate fake data using MultiScale Generator:

$$\tilde{x}_i = G(z_i, y_i; \theta_g)$$

Update Discriminator:
Compute discriminator loss:

$$L_d = -\frac{1}{m}\sum_{i=1}^{m}\left[\log D(x_i, y_i; \theta_d) + \log(1 - D(\tilde{x}_i, y_i; \theta_d))\right]$$

Update θ_d: $\theta_d \leftarrow \theta_d - \eta_d \nabla_{\theta_d} L_d$
Update Generator:
Sample another mini-batch of noise samples $\{z_i\}_{i=1}^{m}$ and labels $\{y_i\}_{i=1}^{m}$
Generate fake data using Multi-Scale Generator:

$$\tilde{x}_i = G(z_i, y_i; \theta_g)$$

Perform Multi-Scale Feature Extraction:
Extract features at multiple scales using convolutional operations to capture diverse spatial and contextual information.
Feature Fusion:
Combine multiscale features along the channel dimension and apply feature fusion techniques to integrate the extracted information.
Refine Output through Convolutional Blocks:
Upsample the fused features using transposed convolutional operations to generate the final output:

$$\hat{x}_i = \mathrm{Refine}(f_{\mathrm{fused}})$$

Compute generator loss:

$$L_g = -\frac{1}{m}\sum_{i=1}^{m}\log D(\hat{x}_i, y_i; \theta_g)$$

Update θ_g: $\theta_g \leftarrow \theta_g - \eta_g \nabla_{\theta_g} L_g$
end for
Output: Conditioned Multi-Scale Generator $G(z, y; \theta_g)$

framework enhances feature extraction efficiency, particularly when dealing with small sample datasets, by incorporating multiscale convolutional layers. These layers significantly improve the network's ability to learn spatial and contextual features across multiple scales, which is essential for generating high-fidelity images that accurately reflect real-world fault conditions. The adoption of c-MSGANs presents several notable advantages.

1) The multiscale feature extraction and fusion in c-MSGANs enhance the quality and diversity of generated images, enabling the model to effectively capture complex fault patterns. This enhances the realism and variability of synthetic samples, thus reinforcing the fault detection model.
2) c-MSGANs mitigate the instability associated with traditional GANs by integrating multiscale processing and feature fusion techniques, providing structured feedback to both the generator and discriminator networks. This approach ensures more stable training, accelerated convergence, and generation of higher-quality synthetic data.
3) c-MSGANs produce high-quality synthetic fault samples, significantly improving the generalization capability of fault detection models. The combination of synthetic and real data helps reduce overfitting, allowing models to perform effectively on unseen data, thereby enhancing real-world applicability.

By employing c-MSGANs, we achieve a robust and practical methodology for augmenting fault datasets, substantially improving fault detection performance through precise feature extraction and high-resolution synthetic image generation. Consequently, this method supports the development of more reliable and efficient fault diagnosis systems.

C. Fault Diagnosis by CNN

CNN have shown remarkable performance in image classification tasks, making them suitable for fault diagnosis using the time-frequency representations generated in the data preprocessing step. This section details the training process of CNN and the evaluation metrics employed.

1) Training Process: The CNN is trained using the labeled dataset, which includes both real and augmented samples generated by the c-MSGANs. The training process involves the following steps.

1) Data Augmentation: The c-MSGANs are used to generate extra training samples to tackle the challenge of limited labeled data.
2) Training: Train the CNN using the augmented dataset. The loss function used is categorical cross-entropy, defined as

$$L(y_i) = -\frac{1}{N}\sum_{i=1}^{N}\sum_{c=1}^{C} y_{ic}\log\left(\hat{y}_{ic}\right) \tag{8}$$

where N is the number of samples, C is the number of classes, y_{ic} is the binary indicator (0 or 1) if class label c is the correct classification for sample i, and $\hat{y}_{ic}$ is the predicted probability for class c for sample i.

3) Optimization: Use Adaptive Moment Estimation (Adam) optimizer to update the model parameters.

2) Discussion on Model Selection: Although more complex architectures such as multiscale CNNs (MSCNNs) have been proposed in previous studies for fault diagnosis [34], in this work, we deliberately choose a relatively simple CNN as the diagnostic backbone. This decision is motivated by the following considerations.

1) *Model Fairness:* Using a standard CNN allows us to better isolate and evaluate the contribution of our proposed c-MSGANs framework without additional confounding factors introduced by model complexity.
2) *Computational Efficiency:* Compared with MSCNN, the simpler CNN model offers advantages in terms of lower computational cost and reduced risk of overfitting, which is important in small-sample learning scenarios.

Therefore, CNN is selected as a lightweight and representative baseline to demonstrate the effectiveness of the proposed data augmentation method. The approach is also applicable to more complex models like MSCNN, where similar performance gains can be observed.

3) Evaluation Metrics: The performance of the trained CNN is evaluated using the following metrics.

1) *Accuracy:* The ratio of correctly predicted samples to the total number of samples, defined as follows:

$$\mathrm{Acc} = \frac{\sum_{i=1}^{i=C} c_{ii}}{\sum_{i=1}^{i=C}\sum_{j=1}^{j=C} c_{ij}} \tag{9}$$

where c_{ij} is the number of samples that belong to the i^{th} category but are predicted as the jth category. C is the number of categories.

2) *Area Under the Curve (AUC):* AUC represents the area under the receiver operating characteristic (ROC) curve, which measures the tradeoff between the true positive rate (TPR) and false positive rate (FPR). A higher AUC indicates better classification performance and a stronger ability to distinguish between different fault classes.
3) *Precision and Recall:* Precision and recall provide insights into the model's classification capability, particularly for imbalanced datasets

$$\mathrm{Precision} = \frac{TP}{TP + FP} \tag{10}$$

$$\mathrm{Recall} = \frac{TP}{TP + FN} \tag{11}$$

where TP, FP, and FN denote the true positives, false positives, and false negatives, respectively. A higher precision reflects fewer false positives, while a higher recall indicates fewer false negatives, both of which are critical in fault diagnosis applications.
4) *Confusion Matrix:* A confusion matrix is used to visualize the classification performance and to understand the types of errors made.

By leveraging the augmented dataset generated by c-MSGANs and CNN, the proposed methodology aims to achieve high accuracy and robustness in fault diagnosis tasks.

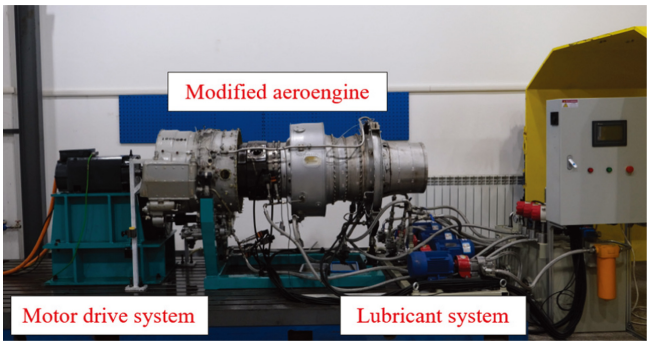

Fig. 3. Test rig of HIT based on a real aero-engine.

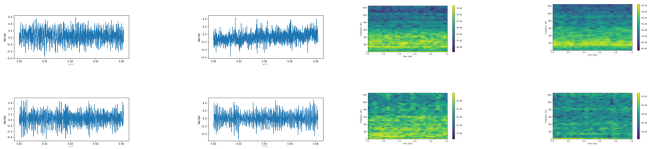

Fig. 4. Comparison of exemplar waveforms and spectrograms before and after STFT. (a) Exemplar waveforms. (b) Exemplar spectrograms.

IV. Experimental Results

In this section, two experimental, one from Harbin Institute of Technology (HIT) bearing dataset which comes from a aero-engine test with intershaft bearing fault and the other from ZHS-2 rotating machinery dataset, are conducted to validate the feasibility and effectiveness of the proposed c-MSGANs-CNN for fault diagnosis under small samples.

A. Case 1: HIT Dataset

1) Dataset Description: The fault diagnosis dataset we used in this case are all from the test rig of HIT [35]. The HIT dataset is sourced from an aero-engine, and this experimental simulation effectively validates the proposed method's efficacy in the aerospace domain. The test rig comprises three main components: 1) a modified aero-engine; 2) a motor drive system; and 3) a lubricant system. The physical map of the test rig is shown in Fig. 3. The raw data are a long time series of 15 s of sampled signals. The sampling frequency is 25000 Hz. After eliminating invalid data, 2412 sets of data are retained in the datasets in total. In the raw data, there are two sets of normal data (N), inner ring fault I (IR I), inner ring fault II (IR II), and outer ring fault (OR).

In the original dataset, the signals from three acceleration channels were collected via sensors positioned at three different locations. For CNN, the diagnosis of faults across multiple channels is typically straightforward. Therefore, we opted to utilize a single channel, mixing data from various measurement points and different rotational speeds to better reflect real-world scenarios. Specifically, the data were segmented into blocks of 2048 data points, ensuring that 1000 samples for each type of fault were reliably obtained. This approach facilitates a more realistic simulation of operational environments for the training of CNN.

TABLE I
Diagnosis Accuracy Under Different Preprocessing Strategies in Case 1

Method	Accuracy (%)
Raw signal + 1D-CNN	92.58
WPD + 2D-CNN	94.17
STFT + 2D-CNN	**95.50**

TABLE II
Detailed Sample Distribution of HIT Dataset Under Different Training Configurations

Description	Training Set		
	2%	4%	6%
Normal condition	14	28	42
Inner ring fault I	14	28	42
Inner ring fault II	14	28	42
Outer ring fault	14	28	42
Total	56	112	168
Testing Set	Total 1200		

Fig. 4 displays the exemplar waveforms and spectrograms before and after STFT. The parameter settings for the STFT are as follows: a Hamming window of length 128 was used, with an overlap of 64, resulting in a 64×32 2-D image. We conducted an ablation by comparing three pipelines: 1) raw vibration signals with a 1-D-CNN; 2) STFT spectrograms with a 2-D-CNN; and 3) WPD representations with the same 2-D-CNN. All experiments used a 7:3 train–test split, a learning rate of 0.01, and 200 epochs, with the CNN architectures configured to maintain comparable model capacity. The results are summarized below to illustrate the relative effectiveness of different preprocessing strategies.

As shown in Table I, both time-frequency approaches achieve higher accuracy than the raw-signal baseline, indicating the advantage of transforming vibration signals into 2-D representations. Among them, STFT attains the best performance, slightly outperforming WPD, which suggests that STFT provides a more suitable balance of time-frequency resolution.

2) Results Analysis and Discussion: The experiments in this article divided the complete sample set into a training set and a testing set at a ratio of 7:3. We conducted experiments using three-fold cross-validation after subsampling the training data at rates of 2%, 4%, and 6%. The distribution of training and testing set sizes under these 2%–6% data configurations is shown in Table II.

During the sample augmentation process, multiple methods were employed for comparison. As referenced in [20], Yang et al. successfully utilized c-GANs to generate high-quality grayscale image samples for bearing fault diagnosis. For comparison, we adopt a c-DCGANs baseline, which employs transposed convolutions in the generator and strided convolutions in the discriminator, with class labels incorporated via conditional embedding. c-DCGANs is widely used for image-like data generation and offers comparable complexity to our c-MSGANs, ensuring a fair baseline for evaluation.

Additionally, we introduced conditional Wasserstein GANs (c-WGANs) as a baseline, following the method described in [36]. This approach provides a more accurate approximation of the distribution between generated and real samples. To further enhance training stability, gradient clipping was employed, significantly mitigating the challenges of instability during GANs training. These adaptations aim to generate higher-quality samples and ensure more stable training compared to traditional GANs variants.

To ensure the validity and fairness of the comparative experiments, the generators and discriminators of all GANs models used for sample augmentation were designed with similar network architectures, except for specific components tailored to each method. This ensured that all models generated pseudo-2-D samples of size 64 $\times$ 32 in the given case study.

In addition, for each class we generated 100 synthetic samples using our augmentation scheme. This number is substantially higher than the original training sample size per class, ensuring that the diagnostic model can leverage a richer set of features extracted from the generated data rather than relying solely on the limited real samples. This strategy not only helps maintain feature consistency and class discriminability, as evidenced by the compact intracluster distributions and distinct intercluster separations in the t-SNE visualizations but also provides qualitative support for the enhanced performance of the c-MSGANs approach over other baseline models.

Fig. 5 presents the *t*-SNE visualisation results for different datasets, providing an intuitive understanding of the data distributions and their inherent characteristics [37]. The visualisation clearly illustrates that synthetic samples generated by the proposed c-MSGANs method align more closely with the real data distribution compared to other generative methods.

The t-SNE visualizations effectively illustrate the comparative performance of different generative methods across varying dataset sizes (2%, 4%, and 6%). For the smallest dataset shown in Fig. 5(a) (2%), the c-MSGANs method (orange clusters) demonstrates notably better alignment with the original training data (blue clusters) compared to both c-DCGANs and c-WGANs. Specifically, the c-MSGANs-generated samples exhibit compact intracluster distributions and clear intercluster separations, effectively capturing the structural characteristics of the original data while maintaining strong class discriminability. As the dataset size increases, as illustrated in Fig. 5(b) and (c), c-MSGANs consistently retain this performance, with tight clusters closely matching the original data distributions. This robustness across varying dataset sizes underscores the capability of c-MSGANs in mitigating data scarcity and preserving distribution integrity, in contrast to the scattered and overlapping clusters produced by c-DCGANs and c-WGANs, which appear to struggle with maintaining class-specific features and structural consistency.

Overall, the t-SNE results clearly demonstrate the enhanced generative capability of c-MSGANs. The method not only increases the diversity of the synthetic samples but also ensures their alignment with the original data distribution, thereby offering potential benefits for fault diagnosis tasks requiring augmented datasets.

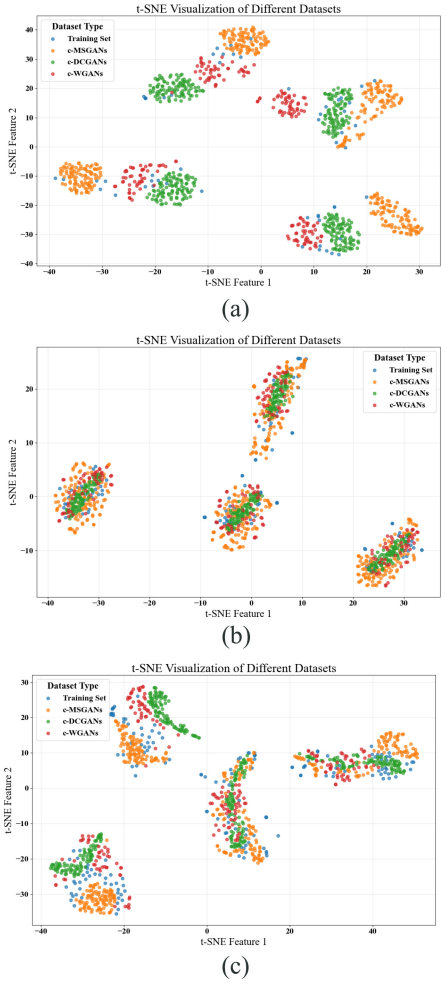

Fig. 5. t-SNE visualization of data distribution for different methods. (a) 2% dataset. (b) 4% dataset. (c) 6% dataset.

TABLE III
DEEP CNN STRUCTURE FOR CUSTOM-CNN

Type	Input Size	Filter	Number	Padding	Stride
Conv1	1×64×32	(2,2)	3	(1,1)	(1,1)
Pool1	3×64×32	(8,4)	-	(0,0)	(8,4)
Conv2	3×8×8	(2,2)	32	(1,1)	(1,1)
Pool2	32×8×4	(8,4)	-	(0,0)	(8,4)
FC1	32×1×2	-	32	-	-
FC2	32	-	4	-	-

To further assess the impact of dataset size on classification performance, we trained the proposed deep CNN model on datasets with varying data volumes. The specific CNN architecture used in each experiment is summarized in Table III. For all CNN models, the training process was conducted for 1000 epochs with a batch size equal to the entire dataset.

To evaluate the effectiveness of the proposed c-MSGANs approach, we compared its performance against baseline models, including CNN, c-WGANs-CNN, and c-DCGANs-CNN, under varying small sample size conditions. As shown in Table IV, the accuracy of c-MSGANs-CNN consistently outperforms other methods across all sample sizes. Specifically, c-MSGANs-CNN achieves a notable improvement, with an accuracy of 91.83% for 2% of the dataset, 96.00% for 4%, and

TABLE IV
ACCURACY OF DIFFERENT MODELS UNDER HIT DATASET

Model	Sample Size (Number)		
	2%	4%	6%
CNN	0.6992	0.8067	0.8233
MSCNN	0.9133	0.9683	0.9708
c-WGANs-CNN	0.8525	0.9017	0.9492
c-DCGANs-CNN	0.9075	0.9450	0.9500
c-MSGANs-CNN	0.9183	0.9600	0.9725
c-MSGANs-MSCNN	0.9658	0.9867	0.9933

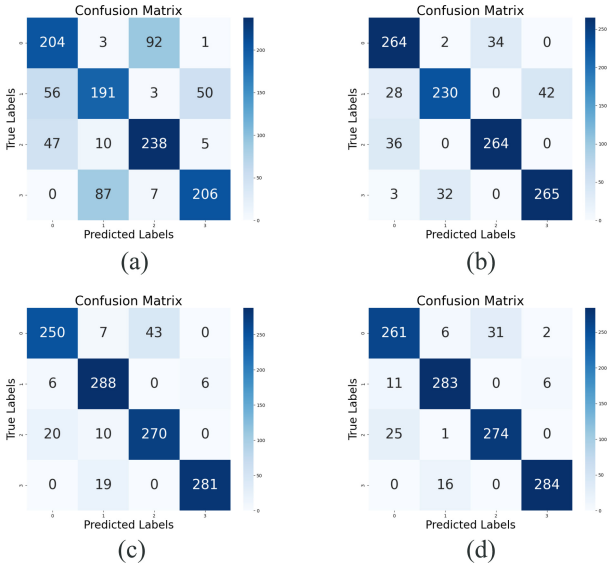

Fig. 6. Confusion matrices of different methods. (a) CNN. (b) c-WGANs-CNN. (c) c-DCGANs-CNN. (d) c-MSGANs-CNN.

97.25% for 6%. These results demonstrate the method's ability to generate informative synthetic samples that enhance diagnostic performance. In contrast, other GAN-based approaches, such as c-WGANs-CNN and c-DCGANs-CNN, show relatively lower accuracy, suggesting challenges in preserving class-specific features and effectively augmenting the dataset.

Furthermore, to validate the generality of the proposed approach across different diagnostic architectures, we extended the experiments to a CNN variant, namely, the MSCNN. As reported in Table IV, MSCNN alone already delivers stronger performance than the basic CNN, and when combined with our c-MSGANs, the resulting c-MSGANs-MSCNN achieves the highest accuracy among all models. This result highlights that the proposed c-MSGANs can be seamlessly integrated with advanced CNN variants and consistently enhance their diagnostic capability, thereby confirming its applicability beyond a single network structure.

To further illustrate the diagnostic performance of the fault diagnosis models, we present the confusion matrices for each method under a 2% training dataset condition in Fig. 6. These matrices provide detailed insights into the classification accuracy and misclassification patterns of the evaluated models, highlighting the strengths and limitations of each approach.

Table IV summarizes the classification performance of various models on the HIT dataset across different sample sizes. The results indicate that the c-MSGANs-CNN model consistently achieves higher accuracy than the baseline models, including CNN, c-WGANs-CNN, and c-DCGANs-CNN. This suggests that the proposed approach effectively enhances model performance under limited data conditions.

TABLE V
PERFORMANCE METRICS OF DIFFERENT MODELS ON THE HIT DATASET

Model	Precision	Recall	AUC
CNN	0.7018	0.6992	0.9069
c-WGANs-CNN	0.8545	0.8525	0.9718
c-DCGANs-CNN	0.9091	0.9075	0.9856
c-MSGANs-CNN	0.9186	0.9183	0.9890

In the smallest dataset scenario (2% of the data), the c-MSGANs-CNN achieves an accuracy of 91.83%, significantly outperforming c-DCGANs-CNN (90.75%) and c-WGANs-CNN (85.25%). This highlights its robust capacity to generate high-quality synthetic samples that effectively enhance classification performance under limited data conditions. As the dataset size increases, c-MSGANs-CNN continues to outperform its counterparts, achieving 96.00% and 97.25% accuracy with 4% and 6% of the data, respectively.

The confusion matrices shown in Fig. 6 provide deeper insights into the classification results. Compared to CNN, c-WGANs-CNN, and c-DCGANs-CNN, the c-MSGANs-CNN model exhibits significantly fewer misclassifications across all fault classes. Particularly, it excels in accurately identifying minority classes, reflecting its enhanced capability to handle class imbalances and capture subtle fault characteristics.

Table V shows that while the baseline CNN already exhibits commendable diagnostic performance, the incorporation of synthetic samples further enhances its ability to capture subtle fault features from a limited training set. The c-MSGANs-CNN model achieves higher precision, recall, and AUC values, demonstrating that our proposed sample augmentation scheme effectively enriches the training data. This, in turn, enables the CNN to learn more robust and detailed representations, thereby significantly improving diagnostic performance in small-sample scenarios.

The remarkable performance of c-MSGANs-CNN can be attributed to its ability to leverage multiscale generative architectures, which enable it to model intricate fault patterns with higher fidelity. This capability ensures that the generated synthetic samples not only augment the dataset but also enrich its diversity and realism, thereby boosting the classifier's generalization performance. Moreover, the consistent advantage of c-MSGANs-CNN across all dataset sizes highlights its adaptability and reliability, making it a promising approach for fault diagnosis in aerospace applications, especially in data-limited scenarios.

B. Case 2: ZHS-2 Dataset

1) Dataset Description: The fault diagnosis dataset we used in this case are all from the ZHS-2 multifunctional motor platform as shown in Fig. 7. Rotating machinery is an integral part of aeronautical equipment, so this case can effectively illustrate the effectiveness of the proposed method

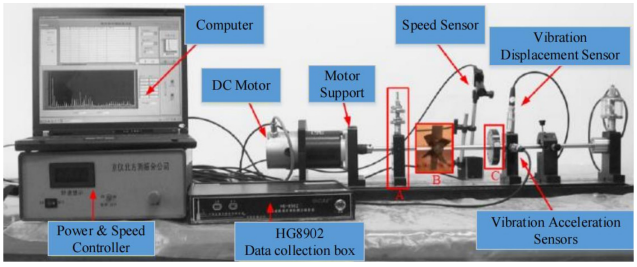

Fig. 7. ZHS-2 type multifunctional motor test bench. A: Pedestal, B: Pan, and C: Rotor.

TABLE VI
DIAGNOSIS ACCURACY UNDER DIFFERENT PREPROCESSING STRATEGIES IN CASE 2

Method	**Accuracy (%)**
Raw signal + 1D-CNN	92.06
WPD + 2D-CNN	95.17
STFT + 2D-CNN	**97.78**

in the aeronautical field. In this experiment, the dataset has six types of faults: 1) Rotor Unbalanced I; 2) Rotor Unbalanced III; 3) Rotor Unbalanced V; 4) Rotor Unbalanced VII; 5) Pedestal Looseness; and 6) the Normal Condition. The four types of Rotor Unbalanced faults are simulated by installing different numbers of screws on the rotor in Fig. 7(C). Fig. 7(C) shows the Rotor Unbalanced V data collected when five screws are installed. The Pedestal Looseness was simulated by loosening the bolts of the pedestal as shown in Fig. 7(A).

During this experiment, the acquisition time of each sample lasts for 8 s, and there were 8 sensors with different positions, each of which recorded 2048 data points. A total of 1000 samples were collected for each fault type and the normal conditions. In order to simulate the actual scenario, we only use the vibration signal captured by the zero sensor. The specific parameter settings for the STFT process in this case are as follows: A Hamming window of length 128 was used, with an overlap of 64, resulting in a 64×32 2-D image. Following the same ablation protocol as in Case 1, we further examined the effect of different preprocessing strategies in Case 2. As summarized in Table VI, both time–frequency methods again surpass the raw-signal baseline, with STFT achieving the best performance, followed by WPD. These results reinforce the conclusion that STFT provides a more effective representation for fault-related features.

2) Results Analysis and Discussion: The distribution of training and testing set sizes under these 2%–6% data configurations is shown in Table VII.

In this case, we use the comparative experimental methods utilized in the previous case and introduce cosine similarity as an evaluation metric to quantify the quality of synthetic samples generated by different networks. Cosine similarity is a measure of the cosine of the angle between two vectors in a multidimensional space, with values ranging between $[-1, 1]$. It evaluates the directional alignment between two vectors, making it particularly suitable for comparing features in high-dimensional data. The mathematical formulation of

TABLE VII
DETAILED SAMPLE DISTRIBUTION OF ZHS-2 DATASET UNDER DIFFERENT TRAINING CONFIGURATIONS

Description	Training Set		
	2%	4%	6%
Normal condition	14	28	42
Unbalanced fault I	14	28	42
Unbalanced fault III	14	28	42
Unbalanced fault V	14	28	42
Unbalanced fault VII	14	28	42
Pedestal Looseness	14	28	42
Total	84	168	252
Testing Set	Total 1800		

TABLE VIII
AVERAGE SIMILARITY OF DIFFERENT DATA SOURCES UNDER DIFFERENT SAMPLE SIZES

Model	Sample Size		
	2%	4%	6%
Real Data(Training set)	0.8203	0.8211	0.8210
Fake Data (Our)	0.8988	0.9633	0.9542
Fake Data (c-WGANs)	0.9642	0.9520	0.9476
Fake Data (c-DCGANs)	0.9068	0.8922	0.8670

cosine similarity is provided in as follows:

$$\text{Cosine Similarity} = \frac{\mathbf{A} \cdot \mathbf{B}}{\|\mathbf{A}\| \|\mathbf{B}\|}. \tag{12}$$

Here, $\mathbf{A}$ and $\mathbf{B}$ represent the vectors being compared, while $|\mathbf{A}|$ and $|\mathbf{B}|$ denote their respective magnitudes. By calculating the cosine similarity between synthetic and real samples, we quantitatively assess the ability of the generative networks to capture the data's underlying feature distributions.

Table VIII illustrates the average cosine similarity values for different data sources under varying sample sizes. These results provide insights into the quality of synthetic samples generated by different generative models when compared with real data.

For synthetic data, our proposed method achieves consistently high similarity scores. Specifically, it attains 0.8988 under 2%, peaks at 0.9633 under 4%, and slightly decreases to 0.9542 under 6%. These results highlight the effectiveness of the proposed c-MSGANs approach in capturing the intrinsic structure of the original data, particularly when training data is limited.

In comparison, c-WGANs demonstrate high performance with similarities exceeding 0.94 across all sample sizes, though there is a slight downward trend as sample size increases. While c-WGANs achieve the highest similarity score under 2%, the marginal drop under larger sample sizes suggests a potential limitation in maintaining data diversity when trained with more data.

On the other hand, c-DCGANs show a notable decline in similarity as sample size increases, dropping from 0.9068 under 2% to 0.8670 under 6%. This indicates a reduced capacity for generating samples that align with the real data

TABLE IX
ACCURACY OF DIFFERENT MODELS UNDER ZHS-2 DATASET

Model	Sample Size (Number)		
	2%	4%	6%
CNN	0.7522	0.8067	0.8789
FD-KNN	0.8228	0.9089	0.9244
c-WGANs-CNN	0.83	0.9061	0.9417
c-DCGANs-CNN	0.7828	0.82	0.9483
c-MSGANs-CNN	0.8767	0.9239	0.9539

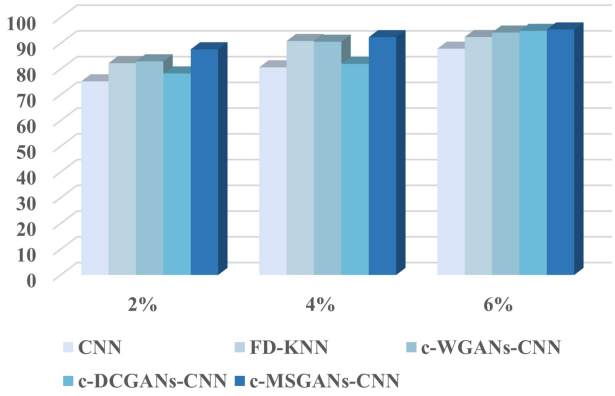

Fig. 8. Prediction accuracy of the all methods in Case 2.

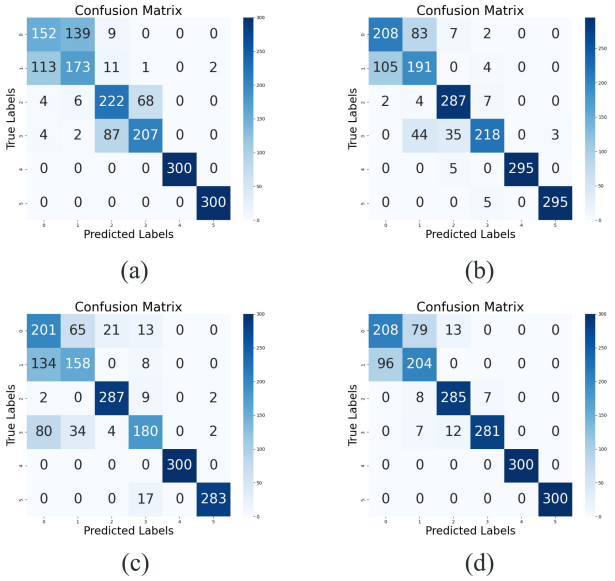

Fig. 9. Confusion matrices of different methods. (a) CNN. (b) c-WGANs-CNN. (c) c-DCGANs-CNN. (d) c-MSGANs-CNN.

distribution, particularly in larger datasets, which may stem from limitations in preserving feature consistency.

Overall, the results highlight the effectiveness of c-MSGANs in maintaining a high degree of similarity with real data across different sample sizes. This robustness, combined with its adaptability under different training conditions, highlights the potential of c-MSGANs for effectively augmenting datasets in fault diagnosis applications.

In this case study, the diagnostic model utilized a CNN architecture that mirrored the structure detailed in Table III, with the sole distinction being the final output layer, which comprised six neurons. Table IX presents the diagnostic accuracy rates achieved on the test set after training convergence for each model under consideration. To further visualize the results, we transformed the data from Table IX into Fig. 8.

In this study, we employed an improved K-nearest neighbor algorithm called FD-KNN. By incorporating feature importance weights into the distance calculation, the method enhances classification accuracy and robustness [38]. In our case study, FD-KNN achieved diagnostic accuracies of 82.28%, 90.89%, and 92.44% for sample sizes of 2%, 4%, and 6%, respectively. Although its performance is slightly lower than the CNN models with c-MSGAN, FD-KNN remains effective in low-data scenarios and serves as a strong baseline for comparison.

The results show that when integrated with the proposed c-MSGANs, the CNN achieves consistently higher accuracy across all sample sizes compared to other models. Notably, the c-MSGANs-CNN model reaches an accuracy of 95.39% with a 6% sample size. This indicates that the synthetic data generated by c-MSGANs closely aligns with real-world data and effectively enhances the diagnostic performance of the CNN model. The improvement is particularly pronounced in scenarios with limited training samples, highlighting the potential of c-MSGANs for dataset augmentation in fault diagnosis applications.

Furthermore, while both c-WGANs and c-DCGANs also improve upon the base CNN's performance, the c-MSGANs-CNN model consistently outperforms them. The relatively lower accuracies observed for c-WGANs and c-DCGANs could be attributed to their limitations in preserving feature consistency or maintaining diversity within the generated data as the sample size increases. These findings collectively highlight the advantages of using c-MSGANs for generating synthetic data in machine learning applications focused on fault diagnosis.

To further evaluate the performance of the different models, we present the confusion matrices for each model under a 2% training dataset condition in Fig. 9.

The CNN model exhibits a relatively balanced distribution across most classes; however, it shows significant misclassifications particularly between classes 1 and 2, as indicated by higher off-diagonal values. The c-WGANs-CNN model demonstrates an improvement over the base CNN, with a reduction in overall misclassifications, suggesting enhanced class separation. Nonetheless, some degree of confusion persists in distinguishing specific classes. Similarly, the c-DCGANs-CNN model also shows improvements over the CNN but still evidences misclassifications. In contrast, the c-MSGANs-CNN model stands out as the highest performer, characterized by the lowest number of misclassifications and very few off-diagonal values, indicative of class separation and classification accuracy.

Table X illustrates that, on the ZHS dataset, the baseline CNN achieves a precision of 75.26%, a recall of 75.22%, and an AUC of 93.99%. In contrast, the c-MSGANs-CNN model significantly improves these metrics, attaining a precision of 87.73%, a recall of 87.67%, and an AUC of 98.14%. These

TABLE X
PERFORMANCE METRICS OF DIFFERENT MODELS ON THE ZHS DATASET

Model	Precision	Recall	AUC
CNN	0.7526	0.7522	0.9399
c-WGANs-CNN	0.8377	0.8300	0.9692
c-DCGANs-CNN	0.7993	0.7828	0.9533
c-MSGANs-CNN	0.8773	0.8767	0.9814

enhancements indicate that the synthetic samples generated by the proposed c-MSGANs method effectively enrich the training data, enabling the CNN to learn more robust and detailed representations even in small-sample scenarios. This further validates the efficacy of our sample augmentation approach in enhancing fault diagnosis performance.

These findings indicate that, while the basic CNN architecture is generally capable of distinguishing between most fault classes effectively, it still encounters difficulty in differentiating closely related classes. Integrating GAN-based approaches, as demonstrated by c-WGANs-CNN and c-DCGANs-CNN, significantly enhances classification precision but does not fully resolve class-specific confusions. The exceptional performance observed with the proposed c-MSGANs-CNN model likely results from its more sophisticated feature-learning mechanism, which substantially improves its ability to discriminate accurately between all classes and reduce misclassification.

Overall, the experimental results from both the HIT and ZHS-2 datasets consistently underline the adaptability, robustness, and effectiveness of the proposed c-MSGANs-CNN method. Its ability to reliably generate realistic and diverse synthetic samples positions it as an effective solution to the data scarcity challenges typically encountered in aerospace fault diagnosis tasks. Therefore, the c-MSGANs-CNN model emerges as a highly promising candidate for real-world fault diagnosis applications, given its accuracy and ability to minimize classification errors.

Although an explicit computational complexity analysis is beyond the scope of the current study, future work will focus specifically on quantifying and optimizing the tradeoff between model complexity and fault diagnostic performance.

V. CONCLUSION

This article proposed a novel approach to address the challenges associated with aerospace fault diagnosis under conditions of severely limited data availability. By employing conditioned multiscale GANs, the method effectively augmented small fault datasets with high-quality synthetic samples. The integration of the STFT during the preprocessing stage successfully preserved critical time-frequency features, thereby enhancing the representation of fault characteristics for diagnosis purposes. Experimental evaluations conducted on two aerospace-related datasets demonstrated that the proposed framework consistently outperformed baseline methods, achieving superior accuracy and robustness, even when trained with severely limited data. In particular, the proposed approach proved highly effective in generating synthetic samples closely aligned with the distributions of real data, as confirmed by visualisation results and quantitative metrics, such as classification accuracy and cosine similarity. Furthermore, the comparative analysis clearly highlighted the benefits of multiscale feature extraction and fusion techniques in improving data diversity and overall diagnostic performance. Overall, this study demonstrated the considerable potential of integrating advanced generative models with CNNs to effectively overcome data scarcity challenges encountered in aerospace fault diagnosis applications. Future research directions were identified, including expanding the applicability of the proposed method to a broader range of aerospace fault scenarios, developing real-time adaptive mechanisms, and exploring the impact of alternative generative network architectures on diagnostic accuracy.

REFERENCES

[1] X. Ma, C. Wen, and T. Wen, "An asynchronous and real-time update paradigm of federated learning for fault diagnosis," *IEEE Trans. Ind. Informat.*, vol. 17, no. 12, pp. 8531–8540, Dec. 2021.

[2] Y. Zheng, W. Li, G. He, K. Ding, and Z. Chen, "Natural modal sketching network: An interpretable approach for bearing impulsive feature extraction," *IEEE Trans. Cybern.*, vol. 55, no. 2, pp. 953–968, Feb. 2025.

[3] H. Jin, Z. Zuo, Y. Wang, L. Cui, and Z. Gao, "Event-triggered interval observer fault detection and isolation for multiagent systems," *IEEE Trans. Cybern.*, vol. 54, no. 7, pp. 4063–4073, Jul. 2024.

[4] T. Chen, C. Zeng, and C. Wang, "Fault identification for a class of nonlinear systems of canonical form via deterministic learning," *IEEE Trans. Cybern.*, vol. 52, no. 10, pp. 10957–10968, Oct. 2022.

[5] Z. Gao, C. Cecati, and S. X. Ding, "A survey of fault diagnosis and fault-tolerant techniques—Part II: Fault diagnosis with knowledge-based and hybrid/active approaches," *IEEE Trans. Ind. Electron.*, vol. 62, no. 6, pp. 3768–3774, Jun. 2015.

[6] K. Zhang, B. Jiang, and M. Staroswiecki, "Dynamic output feedback-fault tolerant controller design for Takagi–Sugeno fuzzy systems with actuator faults," *IEEE Trans. Fuzzy Syst.*, vol. 18, no. 1, pp. 194–201, Feb. 2010.

[7] B. Jiang, K. Zhang, and P. Shi, "Integrated fault estimation and accommodation design for discrete-time Takagi–Sugeno fuzzy systems with actuator faults," *IEEE Trans. Fuzzy Syst.*, vol. 19, no. 2, pp. 291–304, Apr. 2011.

[8] M. Cai, X. He, and D. Zhou, "Self-healing fault-tolerant control for high-order fully actuated systems against sensor faults: A redundancy framework," *IEEE Trans. Cybern.*, vol. 54, no. 4, pp. 2628–2640, Apr. 2024.

[9] C. Ren, B. Jiang, N. Lu, S. Simani, and F. Gao, "Meta-learning with distributional similarity preference for few-shot fault diagnosis under varying working conditions," *IEEE Trans. Cybern.*, vol. 54, no. 5, pp. 2746–2756, May 2024.

[10] H. Ke, Z. Chen, J. Xu, X. Fan, C. Yang, and T. Peng, "Time-frequency hypergraph neural network for rotating machinery fault diagnosis with limited data," in *Proc. IEEE 12th Data Driven Control Learn. Syst. Conf. (DDCLS)*, 2023, pp. 1786–1792.

[11] Z. Zhou, C. Wen, and C. Yang, "Fault isolation based on k-nearest neighbor rule for industrial processes," *IEEE Trans. Ind. Electron.*, vol. 63, no. 4, pp. 2578–2586, Apr. 2016.

[12] T. Chen, Z. Zhu, C. Wang, and Z. Dong, "Rapid sensor fault diagnosis for a class of nonlinear systems via deterministic learning," *IEEE Trans. Neural Netw. Learn. Syst.*, vol. 33, no. 12, pp. 7743–7754, Dec. 2022.

[13] W. Wan, S. He, J. Chen, A. Li, and Y. Feng, "QSCGAN: An unsupervised quick self-attention convolutional GAN for LRE bearing fault diagnosis under limited label-lacked data," *IEEE Trans. Instrum. Meas.*, vol. 70, pp. 1–16, 2021.

[14] T. de Bruin, K. Verbert, and R. Babuška, "Railway track circuit fault diagnosis using recurrent neural networks," *IEEE Trans. Neural Netw. Learn. Syst.*, vol. 28, no. 3, pp. 523–533, Mar. 2017.

[15] W. Yuan, Z. Li, Y. He, R. Cheng, L. Lu, and Y. Ruan, "Open-circuit fault diagnosis of NPC inverter based on improved 1-D CNN network," *IEEE Trans. Instrum. Meas.*, vol. 71, pp. 1–11, 2022.

[16] Y. Qin, Q. Qian, J. Luo, and H. Pu, "Deep joint distribution alignment: A novel enhanced-domain adaptation mechanism for fault transfer diagnosis," *IEEE Trans. Cybern.*, vol. 53, no. 5, pp. 3128–3138, May 2023.
[17] L. Ye, K. Zhang, and B. Jiang, "Synergistic feature fusion with deep convolutional GAN for fault diagnosis in imbalanced rotating machinery," *IEEE Trans. Ind. Informat.*, vol. 21, no. 2, pp. 1901–1910, Feb. 2025.
[18] S. Zhang, S. Wang, Q. Lei, and C. Zhao, "Cross-domain bilateral transfer learning for fault diagnosis under incomplete multisource domains," *IEEE Trans. Autom. Sci. Eng.*, vol. 22, pp. 4298–4310, 2025.
[19] G. Bai, W. Sun, C. Cao, D. Wang, Q. Sun, and L. Sun, "GAN-based bearing fault diagnosis method for short and imbalanced vibration signal," *IEEE Sensors J.*, vol. 24, no. 2, pp. 1894–1904, Jan. 2024.
[20] J. Yang, J. Liu, J. Xie, C. Wang, and T. Ding, "Conditional GAN and 2-D CNN for bearing fault diagnosis with small samples," *IEEE Trans. Instrum. Meas.*, vol. 70, pp. 1–12, 2021.
[21] I. J. Goodfellow et al., "Generative adversarial nets," in *Proc. 27th Int. Conf. Neural Inf. Process. Syst.*, vol. 2, 2014, pp. 2672–2680.
[22] D. Nathani, J. Chauhan, C. Sharma, and M. Kaul, "Learning attention-based embeddings for relation prediction in knowledge graphs," 2019, *arXiv:1906.01195*.
[23] B. Li, X. Qi, T. Lukasiewicz, and P. H. S. Torr, "Controllable text-to-image generation," 2019, *arXiv:1909.07083*.
[24] M. Mirza and S. Osindero, "Conditional generative adversarial nets," 2014, *arXiv:1411.1784*.
[25] Y. LeCun, Y. Bengio, and G. E. Hinton, "Deep learning," *Nature*, vol. 521, pp. 436–444, May 2015.
[26] A. Krizhevsky, I. Sutskever, and G. E. Hinton, "ImageNet classification with deep convolutional neural networks," *Commun. ACM*, vol. 60, no. 6, pp. 84–90, 2012.
[27] D. Huang, W.-A. Zhang, F. Guo, W. Liu, and X. Shi, "Wavelet packet decomposition-based multiscale CNN for fault diagnosis of wind turbine gearbox," *IEEE Trans. Cybern.*, vol. 53, no. 1, pp. 443–453, Jan. 2023.
[28] D. P. Kingma and J. Ba, "Adam: A method for stochastic optimization," 2017, *arXiv:1412.6980*.
[29] J. Zhang, D. Zhang, M. Yang, X. Xu, W. Liu, and C. Wen, "Fault diagnosis for rotating machinery with scarce labeled samples: A deep CNN method based on knowledge-transferring from shallow models," in *Proc. Int. Conf. Control, Autom. Inf. Sci. (ICCAIS)*, 2018, pp. 482–487.
[30] D. Zhong, W. Guo, and D. He, "An intelligent fault diagnosis method based on STFT and convolutional neural network for bearings under variable working conditions," in *Proc. Prognost. Syst. Health Manag. Conf. (PHM-Qingdao)*, 2019, pp. 1–6.
[31] D. Liu, W. Cheng, and W. Wen, "Rolling bearing fault diagnosis via STFT and improved instantaneous frequency estimation method," *Procedia Manuf.*, vol. 49, pp. 166–172, Jul. 2020.
[32] W. Liu, Y. Liu, Z. Zhai, and S. Li, "Time-reassigned multisynchrosqueezing S-transform for bearing fault diagnosis," *IEEE Sensors J.*, vol. 23, no. 19, pp. 22813–22822, Oct. 2023.
[33] Z. Yang, B. He, G. Li, P. Lu, B. Cheng, and P. Zhang, "Multigrained hybrid neural network for rotating machinery fault diagnosis using joint local and global information," *IEEE Trans. Instrum. Meas.*, vol. 72, pp. 1–13, 2023.
[34] G. Jiang, H. He, J. Yan, and P. Xie, "Multiscale convolutional neural networks for fault diagnosis of wind turbine gearbox," *IEEE Trans. Ind. Electron.*, vol. 66, no. 4, pp. 3196–3207, Apr. 2019.
[35] L. Hou et al., "Inter-shaft bearing fault diagnosis based on aero-engine system: A benchmarking dataset study," *J. Dyn., Monitor. Diagn.*, vol. 2, no. 4, pp. 228–242, Aug. 2023.
[36] W. Fu, Y. Chen, H. Li, X. Chen, and B. Chen, "Imbalanced fault diagnosis using conditional Wasserstein generative adversarial networks with switchable normalization," *IEEE Sensors J.*, vol. 23, no. 23, pp. 29119–29130, Dec. 2023.
[37] L. van der Maaten and G. E. Hinton, "Visualizing data using t-SNE," *J. Mach. Learn. Res.*, vol. 9, pp. 2579–2605, Nov. 2008.
[38] S. Zhang, C. Liu, Z. Wang, and S. Liu, "A wind turbine condition monitoring method based on FD-KNN and DLSS active learning strategy," *IEEE Trans. Instrum. Meas.*, vol. 73, pp. 1–18, 2024.

Lihao Ye is currently pursuing the Ph.D. degree in control science and engineering with the College of Automation Engineering, Nanjing University of Aeronautics and Astronautics, Nanjing, China.

His main research interests include machine learning, few-shot learning, federated learning, and fault diagnosis.

Ke Zhang (Senior Member, IEEE) received the Ph.D. degree in control theory and engineering from the Nanjing University of Aeronautics and Astronautics, Nanjing, China, in 2012.

He is currently a Full Professor with the Nanjing University of Aeronautics and Astronautics. He has published three books and over 150 referred international journal papers and conference papers. His research interests include fault diagnosis and fault-tolerant control of dynamical systems and their applications.

Prof. Zhang was a recipient of the Second-Class Prize of the National Natural Science Award of China.

Bin Jiang (Fellow, IEEE) received the Ph.D. degree in automatic control from Northeastern University, Shenyang, China, in 1995.

He has been a Postdoctoral Fellow, a Research Fellow, an Invited Professor, and a Visiting Professor in Singapore, France, USA, and Canada, respectively. He is currently the Chair Professor of Cheung Kong Scholar Program with the Ministry of Education and the Vice President of Nanjing University of Aeronautics and Astronautics, Nanjing, China. He has authored eight books and over 100 referred international journal papers. His current research interests include intelligent fault diagnosis and fault tolerant control and their applications to helicopters, satellites, high-speed aircraft, and high-speed trains.

Prof. Jiang was a recipient of the Second-Class Prize of the National Natural Science Award of China. He currently serves as a Senior Editor for *International Journal of Control, Automation and Systems* and an Associate Editor or an Editorial Board Member for a number of journals, such as the IEEE TRANSACTIONS ON CYBERNETICS, IEEE TRANSACTIONS ON INDUSTRIAL INFORMATICS, IEEE TRANSACTIONS ON NEURAL NETWORKS AND LEARNING SYSTEMS, and *Journal of the Franklin Institute*. He is also the Chair of Control Systems Chapter in IEEE Nanjing Section and a member of IFAC Technical Committee on Fault Detection, Supervision, and Safety of Technical Processes. He is a Fellow of the Chinese Association of Automation.

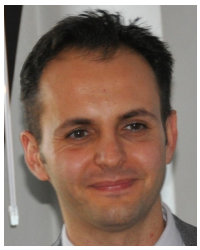

Silvio Simani (Senior Member, IEEE) received the M.Sc. degree in electronic engineering from the University of Ferrara, Ferrara, Italy, in 1996, and the Ph.D. degree in information sciences (automatic control area) from the University of Modena and Reggio Emilia, Modena, Italy, in 2000.

In 2002, he became an Assistant Professor with the Department of Engineering, University of Ferrara, where he has been an Associate Professor since 2014. He has published about 160 refereed journal and conference papers, as well as three books and chapters. His research interests include fault diagnosis, fault-tolerant control, and system identification.

Dr. Simani has been a member of the SAFEPROCESS Technical Committee since 2000.